



Article

Self-Assembled Few-Layered MoS₂ on SnO₂ Anode for Enhancing Lithium-Ion Storage

Thang Phan Nguyen and Il Tae Kim *

Department of Chemical and Biological Engineering, Gachon University,
Seongnam-si, Gyeonggi-do 13120, Korea; phanthang87@gmail.com

* Correspondence: itkim@gachon.ac.kr

Received: 2 December 2020; Accepted: 18 December 2020; Published: 20 December 2020



Abstract: SnO₂ nanoparticles (NPs) have been used as reversible high-capacity anode materials in lithium-ion batteries, with reversible capacities reaching 740 mAh·g⁻¹. However, large SnO₂ NPs do not perform well in charge–discharge cycling. In this work, we report the incorporation of MoS₂ nanosheet (NS) layers with SnO₂ NPs. SnO₂ NPs of ~5 nm in diameter synthesized by a facile hydrothermal precipitation method. Meanwhile, MoS₂ NSs of a few hundreds of nanometers to a few micrometers in lateral size were produced by top-down chemical exfoliation. The self-assembly of the MoS₂ NS layer on the gas–liquid interface was first demonstrated to achieve up to 80% coverage of the SnO₂ NP anode surface. The electrochemical properties of the pure SnO₂ NPs and MoS₂-covered SnO₂ NP anodes were investigated. The results showed that the SnO₂ electrode with a single-layer MoS₂ NS film exhibited better electrochemical performance than the pure SnO₂ anode in lithium storage applications.

Keywords: SnO₂; self-assembly; MoS₂; nanosheets; lithium-ion battery

1. Introduction

The use of lithium-ion batteries (LIBs) helps to solve issues of energy and powering devices in modern life and industries. The prevalence of electronic devices in life and the rapid development of industry have led to a demand for higher-quality energy storage systems with improvements such as higher capacity, greater stability, and improved safety. Currently, commercialized LIBs use lithium–nickel–manganese–cobalt oxide cathodes, which are generally stable but difficult to improve, and graphite anodes, which have a low capacity of ~372 mAh·g⁻¹ [1,2]. The issues requiring attention in the development of LIBs are low anode capacity, degradation, and mechanical instability in LIB structures due to anode material expansion by the insertion and extraction of lithium ions. To improve LIB characteristics, several anode materials have been considered, such as metal alloys, metal oxides, and transition metal chalcogenides (TMCs) [3–5]. Recently, the use of metal oxide materials such as TiO₂, SnO₂, Fe₂O₃, and V₂O₅ for lithium-ion storage anodes has attracted much attention owing to their chemical stability and high reversible capacity [6–15]. Among them, SnO₂ nanoparticles (NPs) have shown promising lithium-ion storage capability with very high capacity reaching 740 mAh·g⁻¹ [16,17]. It has been reported that the required SnO₂ material size is approximately 3 nm to achieve a high reversible capacity [16]. However, the lithiation process of SnO₂ leads to large volume expansion, which results in poor reversible cycling performance [18]. Many methods have been employed to enhance the reaction stability of SnO₂ materials by using carbon-based support materials such as amorphous carbon or graphene, as well as MoS₂. For example, Lou et al. used carbon-supported SnO₂ nanocolloids prepared by a facile hydrothermal method and carbonization [19]. Wang et al. developed a SnO₂–graphene composite material for high-capacity reversible LIBs, which had a capacity of ~440 mAh·g⁻¹ after 100 cycles [20]. Chen et al. reported a composite of SnO₂ and MoS₂

nanosheets (NS) as a LIB anode to diminish the volume expansion during lithiation in SnO₂ NPs [21]. However, the appropriate working conditions and optimization of the SnO₂ morphologies still require investigation and remain challenging in realizing commercial batteries.

Along with the development of metal oxide materials, 2D materials such as graphene and TMCs have drawn great attention owing to their superior properties and flexibility [22–26]. Single- and few-layered TMCs, including MoS₂ and WS₂, have revealed superior electronic and mechanical properties. They have also been utilized in many optical and electrical devices such as solar cells, light-emitting diodes, and transistors, as well as applications in catalysts for hydrogen generation and energy-storage applications in LIBs or sodium-ion batteries [27–30]. MoS₂ in 1T phase has been used to overcome charge–discharge decay and to effectively store lithium or sodium ions with the aid of carbon derivatives such as graphite, carbon nanotubes (CNTs), and graphene. For instance, a combination of CNTs and 1T-structured MoS₂ reported by Nguyen et al. [14] was introduced to develop 3D MoS₂@graphite-CNT for a long-term stable anode material with a very high lithium-ion storage capacity. The 3D-structured MoS₂@graphite-CNT was prepared by a scalable ball-milling method. This 3D structure allowed a high anodic charge–discharge rate and showed a high capacity of ~1200 mAh·g^{−1} after 450 cycles. Moreover, Lane et al. reported the computed electronic structure of lithium- and sodium-intercalated MoS₂. They concluded that the 1T-MoS₂ could be a high-capacity and high-conductivity anode material [31]. Li et al. also discovered that the growth of 3D bulky MoS₂ in the 1T phase supported prolonged anodic cycling, where the structure helped to release strain during cycling and led to improved capacity at high current rates [32]. Therefore, the use of 1T-MoS₂, which has high conductivity and flexibility, can help traditional anode materials exhibit superior performance in lithium storage applications.

In this work, we first demonstrated the use of a 1T-MoS₂ self-assembling layer as protection on the SnO₂ surface. The MoS₂ NS layer was formed by using the gas–liquid interface method, which is well-known for the thin-film preparation of monolayer colloidal crystals such as polystyrene NPs [33–35]. SnO₂ NPs were fabricated by a facile hydrothermal method. The presence of the 1T-MoS₂ layer greatly enhanced the cycling performance of SnO₂ anodes in LIBs. Moreover, the effect of different numbers of MoS₂ layers was also investigated.

2. Experimental

2.1. Chemical Materials

Molybdenum(VI) sulfide (MoS₂, powder), tin(II) chloride dihydrate (SnCl₂·2H₂O, powder), polyvinylidene fluoride (PVDF, M_w 534,000), Sodium dodecylbenzenesulfonate (technical grade) and a 2.5-M solution of *n*-butyllithium in hexane were purchased from Sigma-Aldrich Inc. (St. Louis, MO, USA). Super-P amorphous carbon black (C, approximately 40 nm, 99.99%) and absolute ethanol (C₂H₅OH) were purchased from Alpha Aesar Inc. (Ward Hill, MA, USA). All chemicals were used as delivered without any purification.

2.2. Exfoliation of MoS₂ Nanosheets (NSs)

MoS₂ NSs were synthesized using the liquid chemical exfoliation method [36–38]. In brief, 1 g of MoS₂ powder was placed in a 10-mL vessel. Then, 3 mL of butyllithium in hexane was added to reach the powder level. The solution was kept for 2 days to allow lithium intercalation into the MoS₂ to form Li_{*x*}MoS₂ (*x* > 1) [36,39]. For the exfoliation of MoS₂, Li_{*x*}MoS₂ was washed with hexane to remove excess butyllithium by centrifugation at 5000 rpm for 5 min. The Li_{*x*}MoS₂ obtained was exfoliated in 100 mL deionized (DI) water in a sonication bath for 1 h. The floating large-sized MoS₂ in the solution was removed. Then, 1T-MoS₂ was centrifuged with DI water four times and kept in DI water for further use or dried at 60 °C in a vacuum oven for characterization.

2.3. SnO₂ Nanoparticle (NP) Synthesis

SnO₂ NPs were prepared by a facile hydrothermal method. In a typical synthesis, 0.9 g of SnCl₂·2H₂O was dissolved in 100 mL of DI water under stirring for 30 min. Then, 10 mL of 10% ammonia solution (NH₄OH) was dropped slowly to obtain a gel form. The solution was then transferred to a Teflon autoclave line and heated at 200 °C for 2 h. The white precipitate, SnO₂, was collected via centrifugation and washing for 3 times, then dried and calcinated in air at 600 °C for 1 h.

2.4. Self-Assembled MoS₂ NS Layer

The self-assembled MoS₂ was prepared based on the wettability of the MoS₂ NSs. MoS₂ NSs can be dispersed in DI water; however, an NS floats on the surface of DI water if only one NS surface is wetted. This behavior is similar to that of graphene or polystyrene, both of which can assemble as 2D layers floating on a solution. Here, MoS₂ NSs were dispersed in a 1:1 volumetric DI water–ethanol mixture at a concentration of 2 mg·mL⁻¹. A water bath and half-dipped glass substrate are shown in Figure 1. The prepared solution was then dropped slowly to allow evaporation of the DI water–ethanol solution as the drop met the water surface. The MoS₂ NSs remained randomly floating at the water–air interface. To consolidate the single-layer MoS₂ NSs, a ~10-μL drop of 1% sodium dodecylbenzenesulfonate solution was spread on the surface to increase the surface tension. This formed a semi-transparent layer of MoS₂ on the side of the water bath. The dried anode material was dipped in DI water before it was dipped in the assembled MoS₂ NS layer bath. The MoS₂ NS layers were easily deposited on the electrode surface. Finally, the anode was obtained by drying in a vacuum oven at 70 °C.

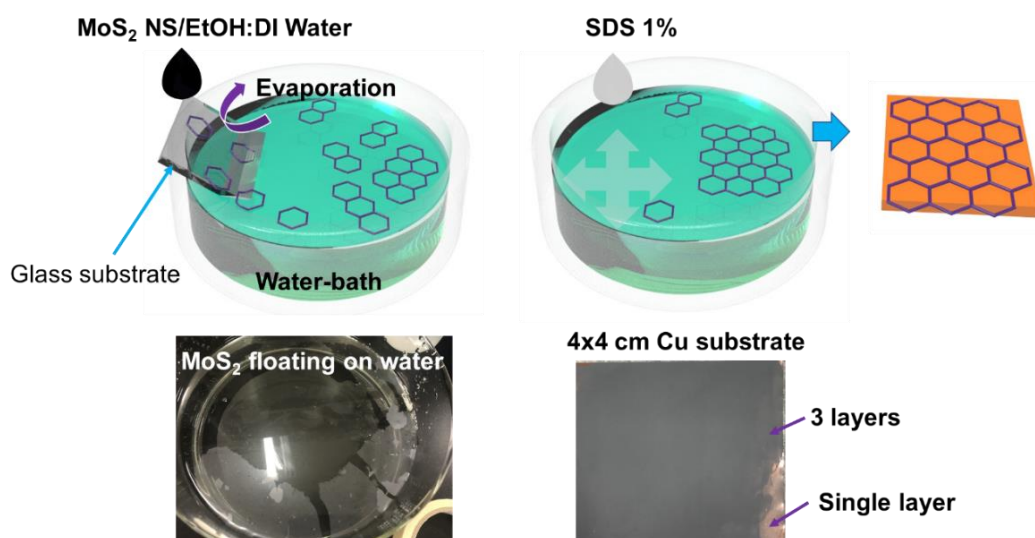


Figure 1. Illustration and photographs of self-assembled MoS₂ nanosheet (NS) on Cu substrate.

2.5. Characterization

X-ray diffraction (XRD) (D/MAX-2200 Rigaku, Tokyo, Japan) was used to investigate the structures of the powder samples. The XRD patterns of the samples were performed over the 2θ range of 10–70°. The structures, morphologies, and sizes of the materials were analyzed by scanning electron microscopy (SEM) (Hitachi S4700, Tokyo, Japan) and transmission electron microscopy (TEM) integrated with energy-dispersive X-ray spectroscopy (EDS) (TECNAI G2F30, FEI Corp., OR, USA).

2.6. Electrochemical Measurements

The SnO₂ NP materials were employed to assemble a half-cell LIB using coin-type cells (CR 2032, Rotech Inc., Gwangju, Korea). The assembly process follows a typical LIB construction method. The working electrode was prepared by pasting a slurry of 70% active material (SnO₂ NP powder),

15% PVDF, and 15% Super P in *N*-methyl-2-pyrrolidinone on a Cu foil by doctor blading. The electrode was then dried in a vacuum oven at 70 °C for at least 12 h before use. The MoS₂ NS layer was lifted from the water surface, as mentioned before, and dried before cell assembly. Electrodes with one, two, and three MoS₂ NS layers were denoted as M1SnO₂, M2SnO₂, and M3SnO₂, respectively. The anodes were punched into circular discs of 12 mm in diameter. The areal loading of active materials was 0.84–1.05 mg cm⁻². The battery half-cell structures were assembled under a neutral gas of Ar in a glovebox with positive pressure to ambient air conditions. The reference electrode, separator, and electrolyte were lithium foil, polyethylene, and 1-M LiPF₆ in ethylene carbonate–diethylene carbonate (1:1 by volume), respectively. The galvanostatic electrochemical charge–discharge performances of the different cells were measured using a battery cycle tester (WBCS3000, WonAtech, Seocho-gu, Seoul) over the voltage range of 0.01–3.0 V versus Li/Li⁺. Cyclic voltammetry (CV) tests and electrochemical impedance spectroscopy (EIS) were performed using a ZIVE MP1 (WonAtech, Seocho-gu, Seoul) over the voltage range of 0.01–3.0 V at a scanning rate of 0.1 mV·s⁻¹ and over the frequency range of 100 kHz–0.1 Hz.

3. Results and Discussion

Figure 2 shows the SEM images of the SnO₂ NP, MoS₂ NS, and SnO₂ anode covered with the MoS₂ NS layer. To prepare the SnO₂ NPs, an easy hydrothermal method was selected to obtain a uniform and highly crystalline material [40–42]. Sn(OH)_x precipitation using NH₄OH solution and hydrothermal processing were applied to develop the crystalline structures of the SnO₂ NPs. It was observed that the size of the NPs was <100 nm. However, the detailed size distribution of the NPs cannot be determined by SEM measurement, as illustrated in Figure 2a,b. The diameters of the SnO₂ NPs are discussed later via TEM analyses. Meanwhile, the MoS₂ NSs were well prepared with lateral sizes ranging from a few hundred nanometers to a few micrometers, as shown in Figure 2c,d. The size of the NSs is larger than that of MoS₂ fabricated by ultrasonication or ball milling [43,44]. The low-magnification SEM image shows that the MoS₂ NSs uniformly cover the Cu electrode. Figure 2e,f shows a single-layer MoS₂ NS thin film on the surface of the SnO₂ electrode. It was calculated that the MoS₂ NSs covered approximately 80% of the SnO₂ electrode surface. The semi-transparent yellow indicates the uncovered electrode surface (Figure 2f), while the dark colors indicate the thin MoS₂ layer covering the surface. From analysis of the SEM images, a novel SnO₂ electrode uniformly covered with MoS₂ NSs layers was prepared, from which better electrochemical performance is expected, compared to that of a pure SnO₂ electrode.

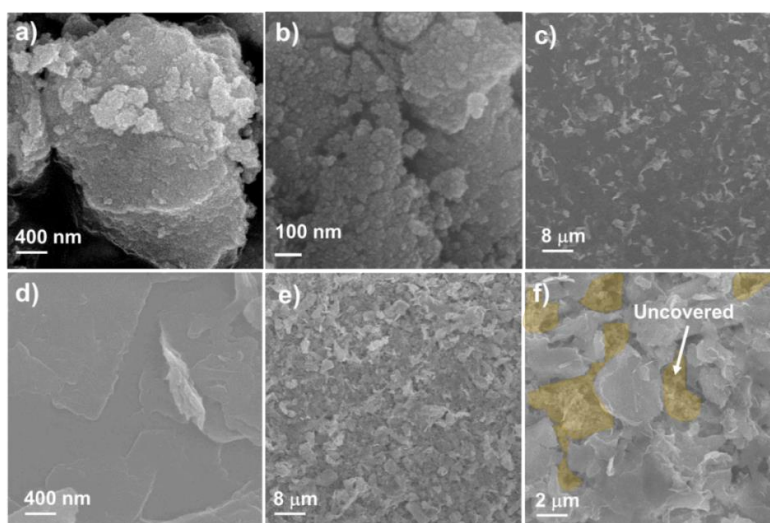


Figure 2. Scanning electron microscope (SEM) images of (a,b) SnO₂ nanoparticle (NP) powder, (c,d) single-layer MoS₂ NS thin film on Cu electrode, and (e,f) M1SnO₂ anode.

To confirm the crystalline nature of the SnO₂ NPs, powder XRD measurements were performed in the range of 10–70°, as shown in Figure 3a. In comparison with PDF #41-1445, the XRD pattern of the SnO₂ NPs was in good agreement with the P4₂/mmn space group [16]. No impurity peaks appear in the pattern. This confirmed the high crystallinity of the SnO₂ NPs. Furthermore, the average sizes of the crystals (D) can be calculated using the Scherrer equation:

$$D = 0.9\lambda/\beta\cos\theta \quad (1)$$

where λ is the X-ray wavelength of the XRD measurement, θ is the Bragg angle, and β is the full width at half maximum of the peak. Based on this information, the calculated crystal size of the SnO₂ NPs was ~2–5 nm. The structure of the assembled MoS₂ layer on SnO₂ anode was also analyzed by XRD as shown in Figure 3a. The peaks of MoS₂ NS, SnO₂ and Cu were clearly revealed, indicating successful coverage of MoS₂ on the SnO₂ anode. Figure 3b shows the XRD patterns of Li_xMoS₂ and the MoS₂ NSs. The intercalation of lithium in the interface of each layer MoS₂ introduced a peak at ~15.4°. After exfoliation in DI water, only the peak of (002) MoS₂ remained, indicating the 2D structure of the MoS₂ NSs. The size of MoS₂ based on the (002) plane was calculated to be ~1 nm, illustrating the formation of thin and single- or few-layered MoS₂ NSs [37,38]. The nanoscale sizes of the SnO₂ NPs are promising for achieving the critical size of SnO₂ that yields the best electrochemical performance. Moreover, high-quality single- and few-layer MoS₂ with large lateral sizes effectively cover the electrode surface.

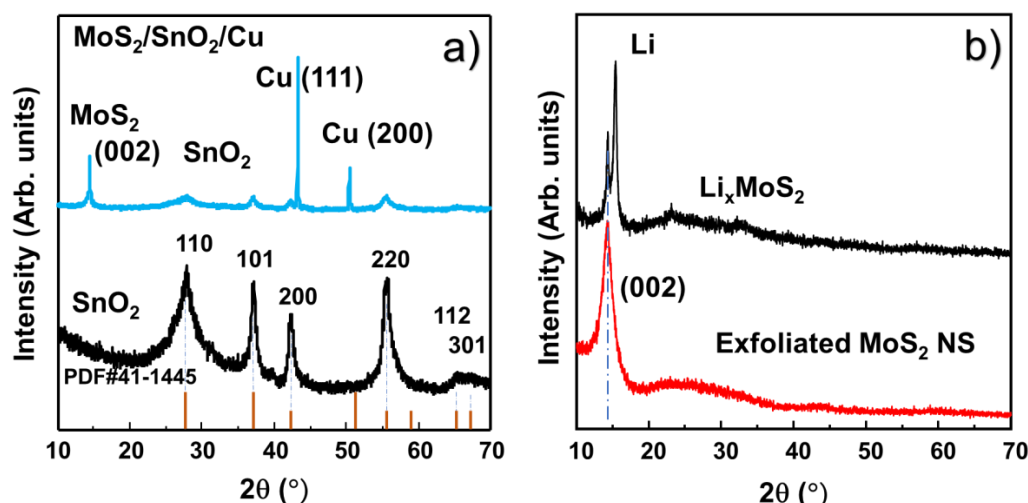


Figure 3. X-ray diffraction (XRD) patterns of (a) SnO₂ NPs and M3SnO₂ anode and (b) lithium-ion intercalated and exfoliated MoS₂ nanosheet.

To further confirm the sizes and structures of the SnO₂ NPs, the SnO₂ powder was observed by TEM. Figure 4a–c shows the SnO₂ EDS mapping images, where clear contrasts indicating Sn and O atoms were detected, indicating the high purity of the synthesized materials. In addition, the high-resolution TEM (HRTEM) image (Figure 4d) clearly shows the lattices of SnO₂ NPs with (101), (110), and (220) planes with sizes of ~5 nm. This result agrees well with the calculation of the SnO₂ crystal size from the XRD patterns. Furthermore, the selected-area electron diffraction (SAED) pattern in Figure 4d also confirms the lattice planes from the crystal structures, as marked with semi-transparent yellow circles. No other elements were found as contaminants. Therefore, pure SnO₂ NPs were well prepared with a diameter of ~5 nm, which would contribute to a high performance in LIBs. Meanwhile, the morphology of MoS₂ NS was also confirmed by HRTEM (Figure 4e), where a lattice spacing of 0.27 nm can be assigned to (100) plane. The spacing between lattice fringes in HRTEM image were to be 1.92 and 3.19 nm for 3 and 5 layers of MoS₂, respectively. Furthermore, the SAED as an inset of

Figure 4e also confirmed the high crystallinity of the MoS₂ layer. Therefore, it can be considered that the MoS₂ NS was successfully exfoliated to single- and few-layer MoS₂.

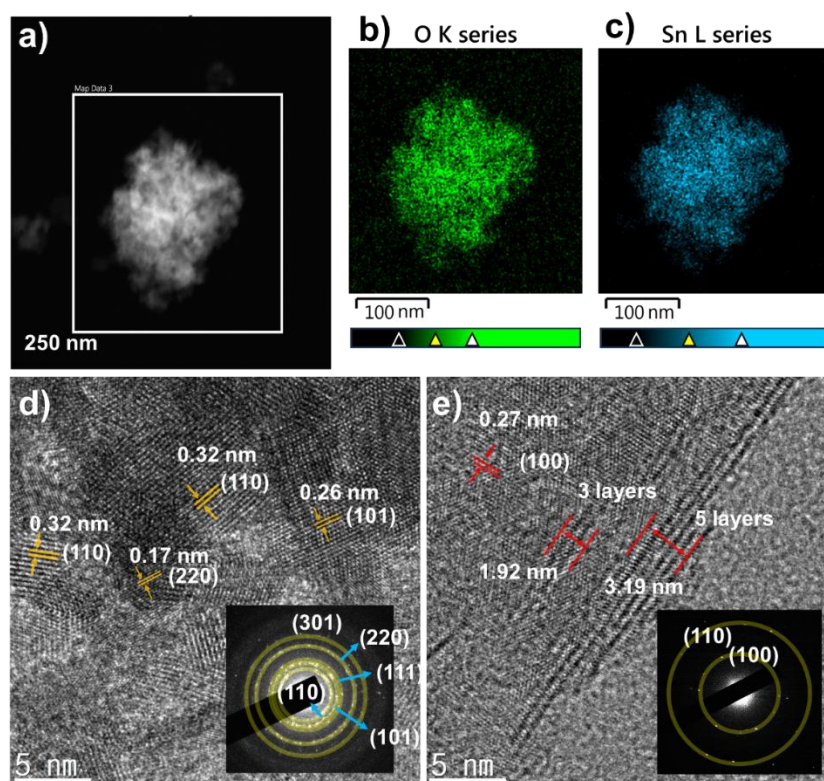
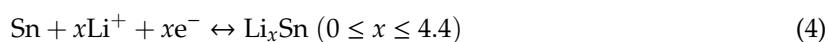


Figure 4. (a) Transmission electron microscope (TEM) image of SnO₂ NP; energy-dispersive X-ray spectroscopy (EDS) mapping of the elements (b) O and (c) Sn; (d) high-resolution TEM (HRTEM) image of SnO₂ NP with inset selected-area electron diffraction (SAED) pattern; (e) exfoliated MoS₂ NS with inset SAED pattern.

To understand the effect of the MoS₂ NS layer on the electrochemical properties of the SnO₂ anode, CV tests were performed between 0.01 and 3.00 V (vs. Li/Li⁺) at a scanning rate of 0.1 mV·s⁻¹. The electrochemical process in the anode can be expressed by the following reaction equations:



Equation (2) relates to the formation of a solid electrolyte (SEI) layer formed from the first lithium-ion insertion. Meanwhile, Equation (3) is the conversion reaction of SnO₂ to Sn. Both reactions (2) and (3) contribute to the irreversible capacity of the anode. Reaction (4) represents the reversible reaction of Sn with lithium ions. Figure 5a shows the electrochemical performance of the pure SnO₂ anode in the initial three cycles. The peak at ~0.84 V in the first cathodic cycle is attributed to the reduction of SnO₂ to Sn metal and the formation of the SEI layer, as illustrated in Equations (2) and (3). In the 2nd and 3rd cycles, these peaks showed reduced intensity and were shifted to the lower potential of ~0.75 V. In the oxidation process, two peaks appear at approximately 0.67 and 1.30 V. Interestingly, the oxidation peak at 0.67 V increases in intensity as the cycle number was increased. This phenomenon could be explained by the activation of the reversible reaction that occurred in the electrode materials [17]. Meanwhile, the oxidation peak at 1.30 V was ascribed to the oxidation

of metallic Sn to SnO₂, which is the reversible case of reaction (2) [17,20,45]. When the MoS₂ NS layer was added to the SnO₂ anode surface, the CV profiles changed depending on the number of layers, as shown in Figure 5b–d, respectively. First, it is easily observed that the oxidation peaks remain stable, with two peaks at 0.67 and 1.30 V related to the reversible reduction and oxidation reaction of Sn metal. With the M1SnO₂ electrode, additional peaks appeared at ~0.42 V and 0.45 V, arising from the conversion reaction as: $\text{Li}_x\text{MoS}_2 + (4-x)\text{Li}^+ + (4-x)\text{e}^- \rightarrow \text{Mo} + 2\text{Li}_2\text{S}$ and from SEI layer formation on the MoS₂ materials [46–49]. The M2/M3SnO₂ electrodes also have peaks at ~0.42 V; however, the intensities are weaker than that of the M1SnO₂ electrode. This can be explained by the energy barrier of the single-layer MoS₂ for lithium-ion intercalation, which is in the range of ~0.42 to ~0.16 eV. Meanwhile, bulk or multilayer MoS₂ has an intercalation energy barrier between 0.73 and 0.59 eV. Therefore, the peaks in the M2/M3SnO₂ electrodes were divided by a small peak at 0.42 V and a joined peak in the range of 0.75–0.84 V of SnO₂ [50]. In addition, the peak intensity at ~0.8 V related to the reduction of SnO₂ increased compared to those of the pure SnO₂ and M1SnO₂ electrodes because of the joined peak of the MoS₂ multilayer. Therefore, it is thought that the addition of MoS₂ NS (two and three layers) might lead to the formation of a large SEI layer. Further, the direct contact of each NS layer can increase the possibility of restacking of the MoS₂ NSs, leading to thicker and bulky MoS₂ NS structures.

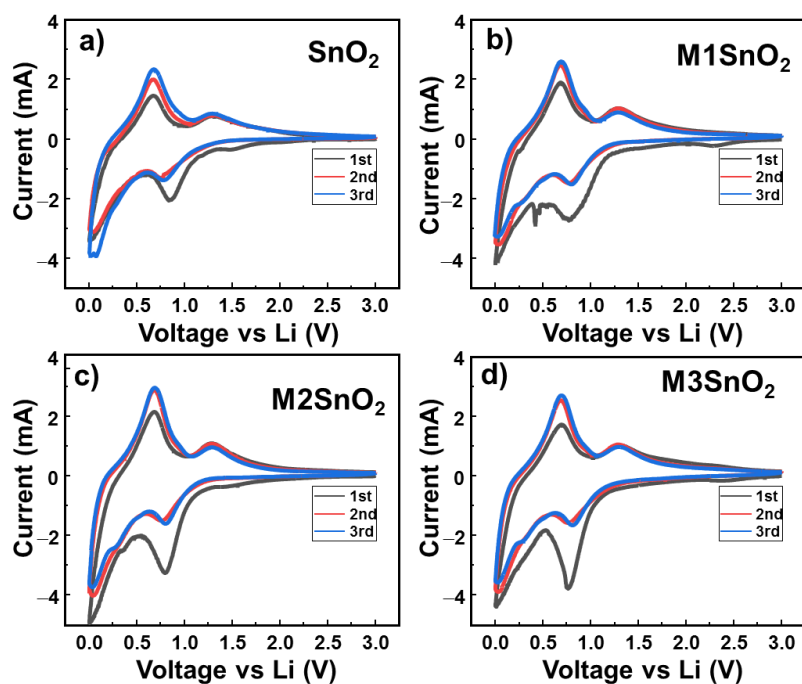


Figure 5. Cyclic voltammetry (CV) profiles of (a) SnO₂ NS and (b–d) M1/M2/M3SnO₂ anodes over three cycles.

The initial voltage profiles of the SnO₂ and M1/M2/M3SnO₂ electrodes at 100 mA·g^{−1} from 0.01 to 3.0 V are shown in Figure 6. The initial discharge capacity of SnO₂ showed a very high value of ~1760 mAh·g^{−1}. This was dramatically reduced to ~880 and ~760 mAh·g^{−1} for the 2nd and 3rd discharges, respectively, indicating a large irreversible reaction due to the formation of an SEI layer and an initial coulombic efficiency (ICE) of 42.3%. However, in the case of the M1SnO₂ electrode (Figure 6b), the 1st, 2nd, and 3rd cycles exhibited slow decreases in the discharge/charge capacities from 1740/760 mAh·g^{−1} to 932/755 mAh·g^{−1} and 835/710 mAh·g^{−1}, respectively. Figure 6c shows the voltage profile of the M2SnO₂ electrode. It shows the 1st discharge/charge capacity of 1730/823 mAh·g^{−1}, corresponding to an ICE of 47.6%. Therefore, it is thought that the better coverage of the MoS₂ NS double layer improved the charge capacity from 760 to 823 mAh·g^{−1} compared to that of the

M1SnO₂ electrode in the first cycle. However, from the next cycle, the capacity was reduced rapidly to 580 mA·h·g⁻¹ in the 3rd cycle. Similarly, the additional coating layer on SnO₂ (M3SnO₂) caused a significant reduction in the discharge/charge capacity in the 1st cycle to 1640/701 mA·h·g⁻¹, which was decreased to ~700/580 mA·h·g⁻¹ in the 3rd cycle. In summary, the addition of MoS₂ layers to the SnO₂ electrode improved the electrochemical performance. However, thicker MoS₂ NSs in excess of two layers decreased the lithium storage capability. This could be explained by the restacking of the MoS₂ NS layers, leading to the formation of bulky or thicker layers. Moreover, TMC materials such as MoS₂ and WS₂ have been reported to improve the electronic properties when present as very thin single- or few-layer structures [31]. This information is in good agreement with the single-layer MoS₂ NS-coated SnO₂ meeting the requirements of enhancing the storage ability, whereas multilayer MoS₂ NS-coated SnO₂ showed faster degradation in battery performance.

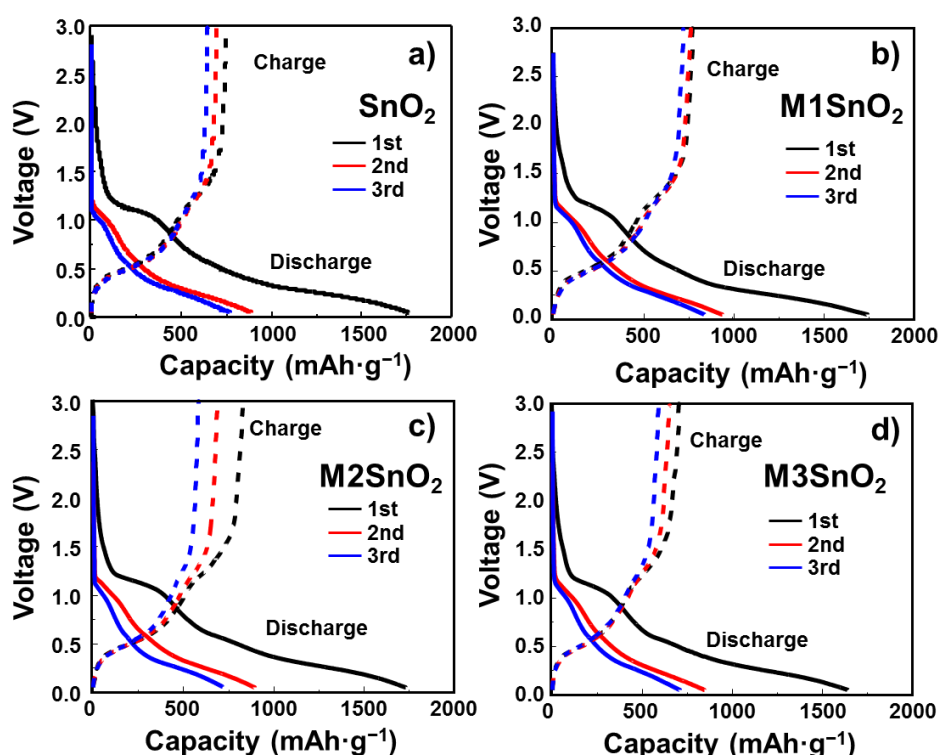


Figure 6. Galvanostatic charge–discharge profiles of (a) SnO₂ NS and (b–d) M1/M2/M3SnO₂ anodes for the initial three cycles.

To evaluate the long-term cyclability, the LIB half-cell with and without the MoS₂ NS layer on the SnO₂ surface were subjected to 100 charge–discharge cycles at a current rate of 100 mA·g⁻¹, as shown in Figure 7a–c. The mass in all measurements was calculated as the real mass of active materials, including SnO₂ and MoS₂, in the electrode. The pure SnO₂ anode showed a substantial decrease in the discharge/charge capacity from 1750/745 mA·h·g⁻¹ to 373/345 mA·h·g⁻¹ at the 10th cycle and to 74.4/73.9 mA·h·g⁻¹ at the 100th cycle, as illustrated in Figure 7a. With the addition of the MoS₂ NS layer, the cyclic stability of lithium storage was much higher than that of the bare electrode. With a similar initial discharge/charge capacity of 1740/760 mA·h·g⁻¹, at the 10th cycle, they exhibited those of 593/551 mA·h·g⁻¹ and retained those of 281/277 mA·h·g⁻¹ at the 100th cycle. It is well observed that the coulombic efficiency retained a high value of ~99%, as shown in Figure 7b. The electrode with >2 layers of MoS₂ NSs showed the worst cyclic performance, retaining a discharge/charge capacity of only 103/102 mA·h·g⁻¹ at the 100th cycle (Figure 7c). Furthermore, the charge-transfer resistance of the cells was measured from the EIS analysis, as depicted in Figure 7d. The modified Randles equivalent circuit was determined to contain a series resistance (R_s), a charge-transfer resistance (R_{ct}),

an SEI resistance (R_{SEI}), and a Warburg impedance element (W) (Figure 7d inset) [4]. The extracted values of these resistances are shown in Table 1. It is easy to observe that the bare SnO_2 has the lowest charge-transfer resistance of $\sim 23.86 \Omega$, while an increasing number of MoS_2 NS layers corresponded to increased charge-transfer resistance in the electrodes. In contrast, the R_{SEI} was dramatically reduced from 500.2Ω in the SnO_2 NP electrode to 182.7Ω in the M1SnO_2 electrode, and then slightly increased to 284.8Ω and 305.1Ω for the M2 and M3SnO_2 electrodes, respectively. The MoS_2 layer provides a large uniform surface compared to that of bare SnO_2 , thus reducing R_{SEI} . Moreover, as discussed above, the electrode with single-layer MoS_2 has a low lithium intercalation energy barrier of $\sim 0.42 \text{ eV}$, while the electrodes with thicker layers have the higher energy barrier of $\sim 0.73 \text{ eV}$. This could lead to an increase in the R_{SEI} . Based on the aforementioned results, the single layer of MoS_2 NS is important in reducing the SEI resistance, thus helping the long-term cycling stability of the SnO_2 anode for lithium storage. This study suggests that coverage of SnO_2 NPs with a thin and complete large-scale MoS_2 layer can significantly enhance the electrode performance in LIBs.

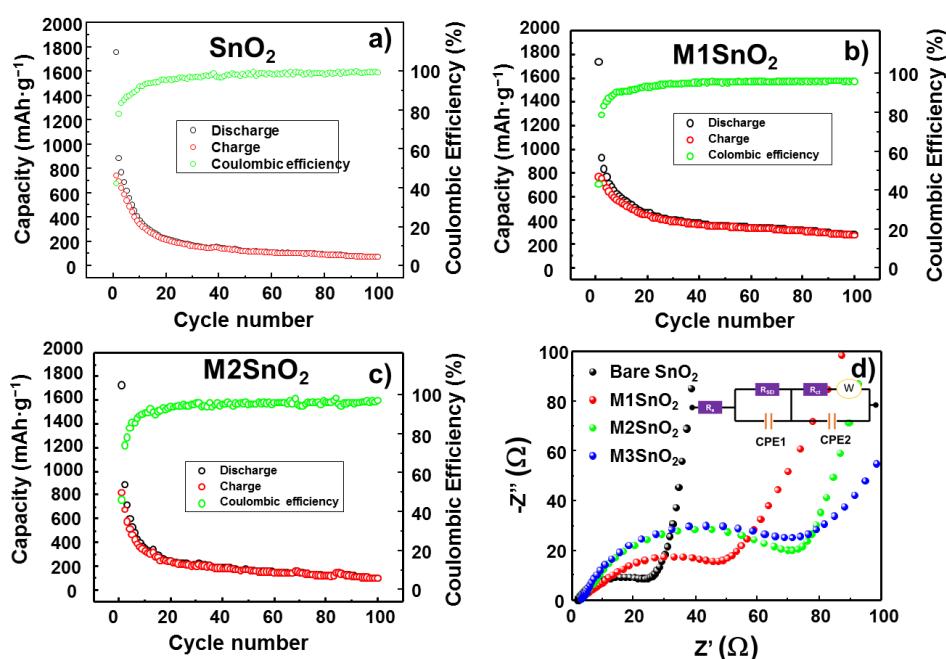


Figure 7. Cyclic performances and Nyquist plots of (a) SnO_2 NPs and (b–d) M1/M2/M3SnO_2 anodes.

Table 1. Resistance values extracted from the equivalent circuit of M1/M2/M3SnO_2 anodes.

Sample	R_s (Ω)	R_{ct} (Ω)	R_{SEI} (Ω)
SnO_2 NPs	1.9	23.8	500.2
M1SnO_2	2.4	59.3	182.7
M2SnO_2	2.8	76.2	284.8
M3SnO_2	2.8	86.1	305.1

The rate cycling performance of the bare SnO_2 and M1SnO_2 electrodes was also investigated, as shown in Figure 8. Performance was recorded for 20 cycles each at charge rates of 100, 500, and $1000 \text{ mA}\cdot\text{g}^{-1}$ before the charge rate returning to $100 \text{ mA}\cdot\text{g}^{-1}$. The SnO_2 electrode shows greater degradation in specific capacity retention when the scan rate is increased. The retentions after 5 cycles at 500 and $1000 \text{ mA}\cdot\text{g}^{-1}$ were 47% and 26%, respectively. In contrast, the M1SnO_2 electrode shows a smaller decrease in specific capacity retention compared to that of pure SnO_2 , where the retentions at 500 and $1000 \text{ mA}\cdot\text{g}^{-1}$ were 70% and 47%, respectively, thus demonstrating much better rate performance than the SnO_2 electrode did. The restoration of the M1SnO_2 electrode when the current rate was decreased from 1000 to $100 \text{ mA}\cdot\text{g}^{-1}$ was also remarkable, corresponding to 95%, far exceeding that

(55%) of the SnO₂ electrode. These results suggest that the introduction of a single MoS₂ layer on SnO₂ electrodes could further enhance the electrochemical performance.

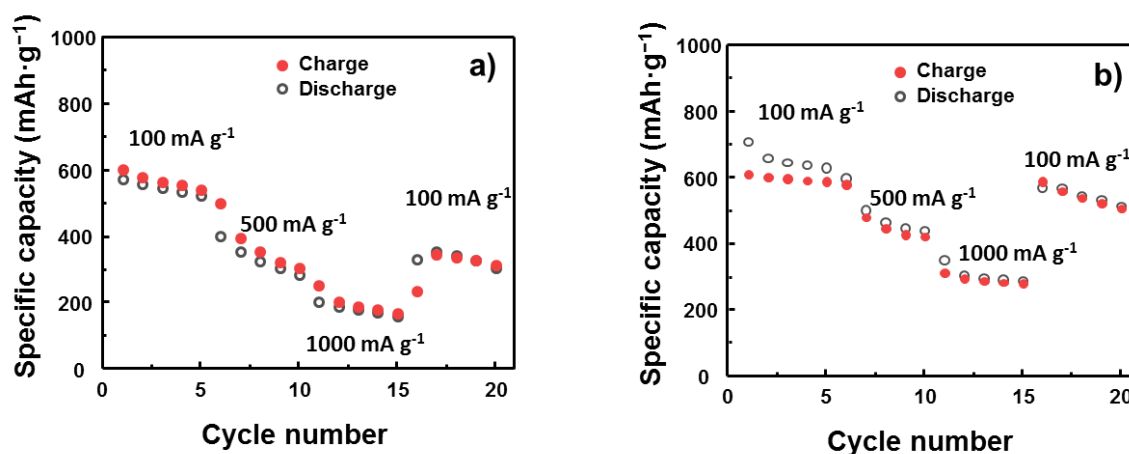


Figure 8. Rate cycling performance of (a) bare SnO₂ electrode and (b) M1SnO₂ electrode at different current rates.

To further confirm the effect of the MoS₂ layer, the surface of the electrode was characterized by ex situ SEM, as shown in Figure 9. The assembled half-cells were run for 10 cycles, and then they were disassembled, washed carefully with dimethyl carbonate and acetone, and dried. Figure 9a,d clearly show that the bare SnO₂ electrode was easily broken, creating micro-holes on the surface. However, the M1SnO₂ electrode was protected from washing, as illustrated in Figure 9b,e. This indicates that the MoS₂ layer can facilitate the formation of a stable and smooth SEI layer. In Figure 9c,f, the M3SnO₂ electrode after 10 cycles shows a thick MoS₂ surface that is much rougher than that of the M1SnO₂ surface. This would be due to the restacking of the MoS₂ NS into a bulky multilayer state. Based on the results, a thin MoS₂ coating layer acted as a protecting layer and formed a uniform SEI layer. The multiple MoS₂ NS layers generated thick and rough surfaces, leading to inferior electrochemical performance for lithium-ion storage.

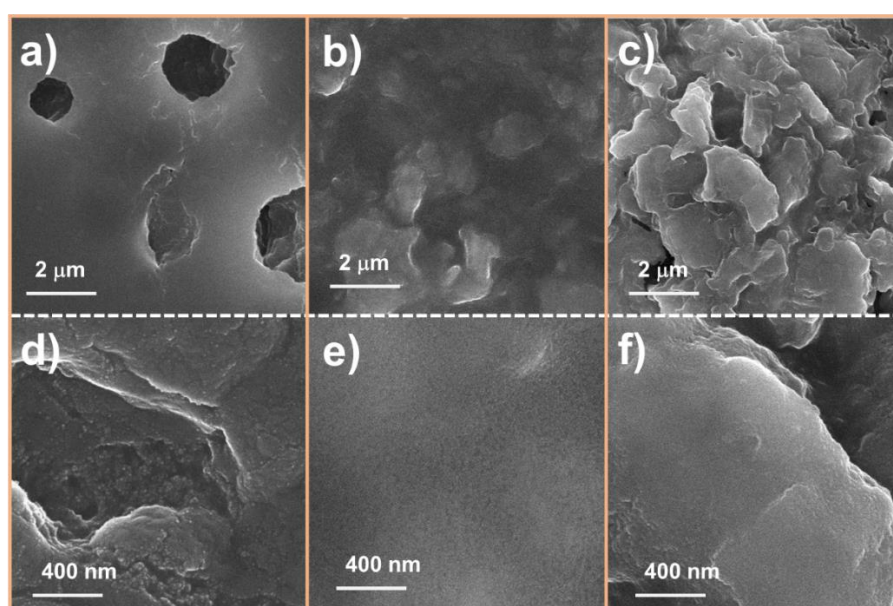


Figure 9. SEM images of (a,d) SnO₂ electrode, (b,e) M1SnO₂ electrode and (c,f) M3SnO₂ electrode after 10 cycles at different magnifications.

4. Conclusions

In summary, this study successfully prepared SnO₂ NPs by a facile hydrothermal method and MoS₂ NS using a liquid chemical exfoliation method. The materials were characterized by XRD, SEM, and TEM measurements. The size of the SnO₂ NPs was about 5–10 nm, and the MoS₂ NSs were hundreds of nanometers to a few micrometers in size. A new coating method utilizing the self-assembly of MoS₂ NS thin films was successfully developed based on a rigid water–air interface. The addition of single-layer MoS₂ NSs enhanced the cyclic stability of the SnO₂ anodes for lithium-ion storage with a high coulombic efficiency of ~99% and high charge/discharge capacity of 281/277 mAh·g⁻¹ compared to those with multiple MoS₂ layers after 100 cycles. These results also suggest that single-layer MoS₂ in large-scale fabrication methods, such as chemical vapor deposition, could be applied to further enhance the cyclic stability of anodes in LIBs.

Author Contributions: T.P.N. Conceptualization, Methodology, Validation, Visualization, Writing—review and editing. I.T.K. Project administration, Funding acquisition, Review & editing. All authors have read and agreed to the published version of the manuscript.

Funding: This work was supported by the National Research Foundation of Korea (NRF) grant funded by the Korean government (MSIT) (NRF-2020R1F1A1048335). This research was also supported by the Basic Science Research Capacity Enhancement Project through a Korea Basic Science Institute (National Research Facilities and Equipment Center) grant funded by the Ministry of Education (2019R1A6C1010016).

Conflicts of Interest: The authors declare no conflict of interest.

References

1. Mo, R.; Tan, X.; Li, F.; Tao, R.; Xu, J.; Kong, D.; Wang, Z.; Xu, B.; Wang, X.; Wang, C.; et al. Tin-graphene tubes as anodes for lithium-ion batteries with high volumetric and gravimetric energy densities. *Nat. Commun.* **2020**, *11*, 1374. [[CrossRef](#)] [[PubMed](#)]
2. Asenbauer, J.; Eisenmann, T.; Kuenzel, M.; Kazzazi, A.; Chen, Z.; Bresser, D. The success story of graphite as a lithium-ion anode material—Fundamentals, remaining challenges, and recent developments including silicon (oxide) composites. *Sustain. Energy Fuels* **2020**, *4*, 5387–5416. [[CrossRef](#)]
3. Nguyen, T.P.; Kim, I.T. W₂C/WS₂ Alloy Nanoflowers as Anode Materials for Lithium-Ion Storage. *Nanomaterials* **2020**, *10*, 1336. [[CrossRef](#)] [[PubMed](#)]
4. Vo, T.N.; Kim, D.S.; Mun, Y.S.; Lee, H.J.; Ahn, S.K.; Kim, I.T. Fast charging sodium-ion batteries based on Te-P-C composites and insights to low-frequency limits of four common equivalent impedance circuits. *Chem. Eng. J.* **2020**, *398*, 125703. [[CrossRef](#)]
5. Zhu, J.; Lu, Y.; Chen, C.; Ge, Y.; Jasper, S.; Leary, J.D.; Li, D.; Jiang, M.; Zhang, X. Porous one-dimensional carbon/iron oxide composite for rechargeable lithium-ion batteries with high and stable capacity. *J. Alloys Compd.* **2016**, *672*, 79–85. [[CrossRef](#)]
6. Song, T.; Paik, U. TiO₂ as an active or supplemental material for lithium batteries. *J. Mater. Chem. A* **2016**, *4*, 14–31. [[CrossRef](#)]
7. Nguyen, T.L.; Hur, J.; Kim, I.T. Facile Synthesis of quantum dots SnO₂/Fe₃O₄ hybrid composites for superior reversible lithium-ion storage. *J. Ind. Eng. Chem.* **2019**, *72*, 504–511. [[CrossRef](#)]
8. Wu, Q.L.; Li, J.C.; Deshpande, R.D.; Subramanian, N.; Rankin, S.E.; Yang, F.Q.; Cheng, Y.T. Aligned TiO₂ Nanotube Arrays As Durable Lithium-Ion Battery Negative Electrodes. *J. Phys. Chem. C* **2012**, *116*, 18669–18677. [[CrossRef](#)]
9. Liu, H.; Li, W.; Shen, D.; Zhao, D.; Wang, G. Graphitic Carbon Conformal Coating of Mesoporous TiO₂ Hollow Spheres for High-Performance Lithium Ion Battery Anodes. *J. Am. Chem. Soc.* **2015**, *137*, 13161–13166. [[CrossRef](#)]
10. Jiang, T.; Bu, F.; Feng, X.; Shakir, I.; Hao, G.; Xu, Y. Porous Fe₂O₃ Nanoframeworks Encapsulated within Three-Dimensional Graphene as High-Performance Flexible Anode for Lithium-Ion Battery. *ACS Nano* **2017**, *11*, 5140–5147. [[CrossRef](#)]
11. He, P.; Ding, Z.; Zhao, X.; Liu, J.; Yang, S.; Gao, P.; Fan, L.Z. Single-Crystal alpha-Fe₂O₃ with Engineered Exposed (001) Facet for High-Rate, Long-Cycle-Life Lithium-Ion Battery Anode. *Inorg. Chem.* **2019**, *58*, 12724–12732. [[CrossRef](#)] [[PubMed](#)]

12. Xu, N.; Liang, J.Q.; Qian, T.; Yang, T.Z.; Yan, C.L. Half-cell and full-cell applications of horizontally aligned reduced oxide graphene/V₂O₅ sheets as cathodes for high stability lithium-ion batteries. *RSC Adv.* **2016**, *6*, 98581–98587. [[CrossRef](#)]
13. Nguyen, T.-A.; Lee, S.-W. Bulky carbon layer inlaid with nanoscale Fe₂O₃ as an excellent lithium-storage anode material. *J. Ind. Eng. Chem.* **2018**, *68*, 140–145. [[CrossRef](#)]
14. Nguyen, Q.H.; Choi, J.S.; Lee, Y.C.; Kim, I.T.; Hur, J. 3D hierarchical structure of MoS₂@G-CNT combined with post-film annealing for enhanced lithium-ion storage. *J. Ind. Eng. Chem.* **2019**, *69*, 116–126. [[CrossRef](#)]
15. Nhung Pham, T.; Ko, J.; Khac Hoang Bui, V.; So, S.; Uk Lee, H.; Hur, J.; Lee, Y.-C. Facile two-step synthesis of innovative anode design from tin-aminoclay (SnAC) and rGO for Li-ion batteries. *Appl. Surf. Sci.* **2020**, *532*, 147435. [[CrossRef](#)]
16. Kim, C.; Noh, M.; Choi, M.; Cho, J.; Park, B. Critical size of a nano SnO₂ electrode for Li-secondary battery. *Chem. Mater.* **2005**, *17*, 3297–3301. [[CrossRef](#)]
17. Li, J.; Zhao, Y.; Wang, N.; Guan, L. A high performance carrier for SnO₂ nanoparticles used in lithium ion battery. *Chem. Commun.* **2011**, *47*, 5238–5240. [[CrossRef](#)]
18. Zhao, S.; Sewell, C.D.; Liu, R.; Jia, S.; Wang, Z.; He, Y.; Yuan, K.; Jin, H.; Wang, S.; Liu, X.; et al. SnO₂ as Advanced Anode of Alkali-Ion Batteries: Inhibiting Sn Coarsening by Crafting Robust Physical Barriers, Void Boundaries, and Heterophase Interfaces for Superior Electrochemical Reaction Reversibility. *Adv. Energy Mater.* **2019**, *10*, 1902657. [[CrossRef](#)]
19. Lou, X.W.; Chen, J.S.; Chen, P.; Archer, L.A. One-Pot Synthesis of Carbon-Coated SnO₂ Nanocolloids with Improved Reversible Lithium Storage Properties. *Chem. Mater.* **2009**, *21*, 2868–2874. [[CrossRef](#)]
20. Wang, X.Y.; Zhou, X.F.; Yao, K.; Zhang, J.G.; Liu, Z.P. A SnO₂/graphene composite as a high stability electrode for lithium ion batteries. *Carbon* **2011**, *49*, 133–139. [[CrossRef](#)]
21. Chen, Y.; Lu, J.; Wen, S.; Lu, L.; Xue, J.M. Synthesis of SnO₂/MoS₂ composites with different component ratios and their applications as lithium ion battery anodes. *J. Mater. Chem. A* **2014**, *2*, 17857–17866. [[CrossRef](#)]
22. Kim, C.; Nguyen, T.P.; Le, Q.V.; Jeon, J.M.; Jang, H.W.; Kim, S.Y. Performances of Liquid-Exfoliated Transition Metal Dichalcogenides as Hole Injection Layers in Organic Light-Emitting Diodes. *Adv. Funct. Mater.* **2015**, *25*, 4512–4519. [[CrossRef](#)]
23. Nguyen, T.P.; Le, Q.V.; Choi, K.S.; Oh, J.H.; Kim, Y.G.; Lee, S.M.; Chang, S.T.; Cho, Y.H.; Choi, S.; Kim, T.Y.; et al. MoS₂ Nanosheets Exfoliated by Sonication and Their Application in Organic Photovoltaic Cells. *Sci. Adv. Mater.* **2015**, *7*, 700–705. [[CrossRef](#)]
24. Voiry, D.; Goswami, A.; Kappera, R.; e Silva, C.D.C.C.; Kaplan, D.; Fujita, T.; Chen, M.; Asefa, T.; Chhowalla, M. Covalent functionalization of monolayered transition metal dichalcogenides by phase engineering. *Nat. Chem.* **2015**, *7*, 45–49. [[CrossRef](#)]
25. Castellanos-Gomez, A.; Poot, M.; Steele, G.A.; van der Zant, H.S.J.; Agrait, N.; Rubio-Bollinger, G. Elastic Properties of Freely Suspended MoS₂ Nanosheets. *Adv. Mater.* **2012**, *24*, 772–775. [[CrossRef](#)]
26. Nguyen, T.P.; Kim, S.Y.; Lee, T.H.; Jang, H.W.; Le, Q.V.; Kim, I.T. Facile synthesis of W₂C@WS₂ alloy nanoflowers and their hydrogen generation performance. *Appl. Surf. Sci.* **2020**, *504*, 144389. [[CrossRef](#)]
27. Coleman, J.N.; Lotya, M.; O'Neill, A.; Bergin, S.D.; King, P.J.; Khan, U.; Young, K.; Gaucher, A.; De, S.; Smith, R.J.; et al. Two-dimensional nanosheets produced by liquid exfoliation of layered materials. *Science* **2011**, *331*, 568–571. [[CrossRef](#)]
28. Yu, Y.; Zhang, Y.T.; Song, X.X.; Zhang, H.T.; Cao, M.X.; Che, Y.L.; Dai, H.T.; Yang, J.B.; Zhang, H.; Yao, J.Q. PbS-Decorated WS₂ Phototransistors with Fast Response. *ACS Photonics* **2017**, *4*, 950–956. [[CrossRef](#)]
29. Le, Q.V.; Nguyen, T.P.; Jang, H.W.; Kim, S.Y. The use of UV/ozone-treated MoS₂ nanosheets for extended air stability in organic photovoltaic cells. *Phys. Chem. Chem. Phys.* **2014**, *16*, 13123–13128. [[CrossRef](#)]
30. Nguyen, T.P.; Le, Q.V.; Choi, S.; Lee, T.H.; Hong, S.-P.; Choi, K.S.; Jang, H.W.; Lee, M.H.; Park, T.J.; Kim, S.Y. Surface extension of MeS₂ (Me = Mo or W) nanosheets by embedding MeS_x for hydrogen evolution reaction. *Electrochim. Acta* **2018**, *292*, 136–141. [[CrossRef](#)]
31. Lane, C.; Cao, D.X.; Li, H.Y.; Jiao, Y.C.; Barbiellini, B.; Bansil, A.; Zhu, H.L. Understanding Phase Stability of Metallic 1T-MoS₂ Anodes for Sodium-Ion Batteries. *Condens. Matter* **2019**, *4*, 53. [[CrossRef](#)]
32. Li, S.C.; Liu, P.; Huang, X.B.; Tang, Y.G.; Wang, H.Y. Reviving bulky MoS₂ as an advanced anode for lithium-ion batteries. *J. Mater. Chem. A* **2019**, *7*, 10988–10997. [[CrossRef](#)]
33. Li, C.; Hong, G.S.; Qi, L.M. Nanosphere Lithography at the Gas/Liquid Interface: A General Approach toward Free-Standing High-Quality Nanonets. *Chem. Mater.* **2010**, *22*, 476–481. [[CrossRef](#)]

34. Rybczynski, J.; Ebels, U.; Giersig, M. Large-scale, 2D arrays of magnetic nanoparticles. *Colloids Surf. A-Physicochem. Eng. Asp.* **2003**, *219*, 1–6. [[CrossRef](#)]
35. Li, C.; Hong, G.S.; Wang, P.W.; Yu, D.P.; Qi, L.M. Wet Chemical Approaches to Patterned Arrays of Well-Aligned ZnO Nanopillars Assisted by Monolayer Colloidal Crystals. *Chem. Mater.* **2009**, *21*, 891–897. [[CrossRef](#)]
36. Joensen, P.; Frindt, R.F.; Morrison, S.R. Single-layer MoS₂. *Mater. Res. Bull.* **1986**, *21*, 457–461. [[CrossRef](#)]
37. Eda, G.; Yamaguchi, H.; Voiry, D.; Fujita, T.; Chen, M.; Chhowalla, M. Photoluminescence from chemically exfoliated MoS₂. *Nano Lett.* **2011**, *11*, 5111–5116. [[CrossRef](#)]
38. Park, M.; Nguyen, T.P.; Choi, K.S.; Park, J.; Ozturk, A.; Kim, S.Y. MoS₂-nanosheet/graphene-oxide composite hole injection layer in organic light-emitting diodes. *Electron. Mater. Lett.* **2017**, *13*, 344–350. [[CrossRef](#)]
39. Yang, D.; Frindt, R.F. Li-intercalation and exfoliation of WS₂. *J. Phys. Chem. Solids* **1996**, *57*, 1113–1116. [[CrossRef](#)]
40. Akhir, A.M.; Rezan, S.A.; Mohamed, K.; Arafat, M.M.; Haseeb, A.S.M.A.; Lee, H.L. Synthesis of SnO₂ Nanoparticles via Hydrothermal Method and Their Gas Sensing Applications for Ethylene Detection. *Mater. Today Proc.* **2019**, *17*, 810–819. [[CrossRef](#)]
41. Patil, G.E.; Kajale, D.D.; Gaikwad, V.B.; Jain, G.H. Preparation and characterization of SnO₂ nanoparticles by hydrothermal route. *Int. Nano Lett.* **2012**, *2*, 17. [[CrossRef](#)]
42. Dias, J.S.; Batista, F.R.M.; Bacani, R.; Triboni, E.R. Structural characterization of SnO nanoparticles synthesized by the hydrothermal and microwave routes. *Sci. Rep.* **2020**, *10*, 9446. [[CrossRef](#)] [[PubMed](#)]
43. Han, C.; Zhang, Y.; Gao, P.; Chen, S.; Liu, X.; Mi, Y.; Zhang, J.; Ma, Y.; Jiang, W.; Chang, J. High-Yield Production of MoS₂ and WS₂ Quantum Sheets from Their Bulk Materials. *Nano Lett.* **2017**, *17*, 7767–7772. [[CrossRef](#)] [[PubMed](#)]
44. Nguyen, T.P.; Sohn, W.; Oh, J.H.; Jang, H.W.; Kim, S.Y. Size-Dependent Properties of Two-Dimensional MoS₂ and WS₂. *J. Phys. Chem. C* **2016**, *120*, 10078–10085. [[CrossRef](#)]
45. Reddy, M.V.; Andreea, L.Y.T.; Ling, A.Y.; Hwee, J.N.C.; Lin, C.A.; Admas, S.; Loh, K.P.; Mathe, M.K.; Ozoemena, K.I.; Chowdari, B.V.R. Effect of preparation temperature and cycling voltage range on molten salt method prepared SnO₂. *Electrochim. Acta* **2013**, *106*, 143–148. [[CrossRef](#)]
46. Wu, H.; Hou, C.Y.; Shen, G.Z.; Liu, T.; Shao, Y.L.; Xiao, R.; Wang, H.Z. MoS₂/C/C nanofiber with double-layer carbon coating for high cycling stability and rate capability in lithium-ion batteries. *Nano Res.* **2018**, *11*, 5866–5878. [[CrossRef](#)]
47. Gong, Y.J.; Yang, S.B.; Zhan, L.; Ma, L.L.; Vajtai, R.; Ajayan, P.M. A Bottom-Up Approach to Build 3D Architectures from Nanosheets for Superior Lithium Storage. *Adv. Funct. Mater.* **2014**, *24*, 125–130. [[CrossRef](#)]
48. Gao, S.N.; Yang, L.T.; Shao, J.; Qu, Q.T.; Wu, Y.P.; Holze, R. Construction of Hierarchical Hollow MoS₂/Carbon Microspheres for Enhanced Lithium Storage Performance. *J. Electrochem. Soc.* **2020**, *167*, 100525. [[CrossRef](#)]
49. Cui, C.Y.; Li, X.; Hu, Z.; Xu, J.T.; Liu, H.K.; Ma, J.M. Growth of MoS₂@C nanobowls as a lithium-ion battery anode material. *RSC Adv.* **2015**, *5*, 92506–92514. [[CrossRef](#)]
50. Cha, E.; Patel, M.D.; Park, J.; Hwang, J.; Prasad, V.; Cho, K.; Choi, W. 2D MoS₂ as an efficient protective layer for lithium metal anodes in high-performance Li-S batteries. *Nat. Nanotechnol.* **2018**, *13*, 337–344. [[CrossRef](#)]

Publisher's Note: MDPI stays neutral with regard to jurisdictional claims in published maps and institutional affiliations.



© 2020 by the authors. Licensee MDPI, Basel, Switzerland. This article is an open access article distributed under the terms and conditions of the Creative Commons Attribution (CC BY) license (<http://creativecommons.org/licenses/by/4.0/>).